SCIENTIFIC REPORTS

OPEN

Received: 24 April 2018
Accepted: 17 September 2018
Published online: 27 September 2018

MoB_2 Driven Metallic Behavior and Interfacial Charge Transport Mechanism in MoS_2/MoB_2 Heterostructure: A First-Principles Study

Amreen Bano, Devendra K. Pandey, Anchit Modi & N. K. Gaur

We have performed the density functional theory calculations on heterostructure (HS) of MoS_2 and MoB_2 monolayers. The aim of this study is to assess the influence of MoB_2 on electron transport of adjacent MoS_2 layer. In present investigation we predict that the electronic properties of MoS_2 monolayer is influenced by 4d-states of Mo in MoB_2 monolayer. Whereas, the B atoms of MoB_2 and S atoms of MoS_2 exhibit overlapping of intermediate atomic orbitals thereby collectively construct the interfacial electronic structure observed to be metallic in nature. From charge density calculations, we have also determine that the charge transfer is taking place at the interface via B-2p and S-3p states. The bonds at the interface are found to be metallic which is also confirmed by adsorption analysis. Thermoelectric performance of this HS is found be in good agreement with available literature. Low Seebeck coefficient and high electrical conductivity further confirms the existence of metallic state of the HS.

The family of layered dichalcogenide semiconductor materials such as molybdenum disulfide (MoS_2) has obtained significant attention over the last years as potential candidates for electronic[1–4] and optoelectronic applications[5–7]. These materials consist of stacked quasi two dimensional atomic layers that are physically independent to a large extent and can be separated easily. The combination of two-dimensional (2D) dichalcogenides with other 2D or low dimensional materials, such as graphene[7,8] boron nitride or other dichalcogenides have interesting applications[9]. In principle it provides a completely new class of artificial materials with designed electronic, optical and mechanical properties[10,11]. Tuning of electronic properties of 2D transition metal dichalcogenide (TMD) materials are important for their application in optoelectronics. Monolayer TMDs with formula MX_2 (M = Mo, W; X = S, Se, Te) describes the class of semiconductors with narrow direct band gap, large exciton binding energies, high photoelectrochemical activity and high optoconductivity. Such materials, due to inversion symmetry breaking are used for the study of valley polarization and spin-vally coupling[12,13]. Heterostructures (HSs) are used on a large scale in conventional semiconductors for achieving tunable electronic properties. For the development of future 2D materials, the HSs with Van der Waals interactions have been recognized as promising candidates[14] and TMD-based hybrid multilayered structures are a prototype van der Waals HSs[15]. It has been reported that the protected phosphorene and tunable carrier dynamics and optical properties can be achieved by coupling of phosphorene with stable graphene[16] or hBN[17] and even phosphorene suboxide[18] and organism TiL_4[19]. According to a theoretical study, phosphorene/graphene HS has been proposed as an anode material for rechargeable Li batteries[20]. The phosphorene/MoS_2 HS is a suitable type-II semiconductor for ultraviolet photodetector applications[21]. Moreover, the black-phosphorus/blue-phosphorus HS is predicted to be used in solar energy conversion[22,23]. Rapid transfer of photogenerated charge carriers between $MoSe_2$ and graphene has been found in $MoSe_2$/graphene HSs depicting its applications in optoelectronics[24]; black phosphorene/$MoSe_2$ HS show potential applications in p-n diodes and logical devices[25,26]. Insulating perovskite substrate $SrTiO_3$ has also been coupled with MoS_2 monolayer that shows direct semiconducting band gap and chemisorption of MoS_2 monolayer has been observed[27]. Cathodoluminescence and photon emission excited by a high-energy electron beam can

Department of Physics, Barkatullah University, Bhopal, 462026, India. Correspondence and requests for materials should be addressed to N.K.G. (email: srl_nkgaur@yahoo.co.in)

be applied in the analysis of mineral compositions[28], light emitting diodes[29,30] and surface plasmon mapping[31]. Compared to photoluminescence the cathodoluminescence offers a much higher excitation energy allowing the study of wide band gap materials including diamond[32] and hexagonal boron nitride (hBN)[33]. The thermoelectric (TE) properties in few layer and bulk MoS_2 and MoS_2 monolayer have been theoretically investigated and found to be reasonably good for TE applications[34–37]. TE power factor of 8.5 $mWm^{-1}K^{-2}$ for MoS_2 monolayer at room temperature had been reported by Kedar *et al.* which is the highest among all TE materials and twice that of commercially used bismuth telluride (Bi_2Te_3)[38]. Whereas, for MoS_2 monolayer deposited on substrates, Hasan *et al.* had reported a poor response in the TE power factor[39]. For improving the TE performance of MoS_2 based systems, the hybridization and doping have been commonly explored. Moreover SiGe alloys, hybrid BN/graphene and MoS_2/WS_2 nanoribbons show higher thermoelectric properties than single nanostructures[40,41]. We reviewed that the investigation for HSs of MoS_2 with intermetallic material need to be explored. The transition metal diborides XB_2 (X = V, Nb, Ta, Cr, Mo, and W) having hexagonal AlB_2 structure received much attention because for their interesting physical and chemical properties such as electronic structure, high melting point, corrosion resistance, wear resistance, high hardness factor and possibility of extensive industrial applications[16,42–46]. Recently, ReB_2 and OsB_2 has been analyzed for exhibiting high bulk elastic moduli in a particular direction(c-axis) owing to the high valence electron density in the lattice which is comparable to that of diamond[47,48]. Recently it is been reported that lattice mismatches in the cell parameters and comparable thermal expansion with GaN, ZrB_2 can be optimized as a substrate for hetero epitaxial growth of GaN[49,50]. For the reinforcements in various composite materials e.g. steel and TiB_2 has often been used[51,52]. With reference to the above discussion we have motivated to theoretically examine the electronic and thermoelectric properties of MoS_2/MoB_2 HS. We have selected this combination of monolayers due to their interesting electronic properties, specifically the Boron terminated MoB_2 layer with a wide range of thermodynamically allowed chemical potentials[53]. In Section I, we have elaborated the computational details applied to probe several significant features of interfacial electronic structure of MoS_2/MoB_2. The results for electronic structure of HS and isolated sub-systems along with chemisorption, chemical bonding and thermoelectric properties occurring at the interface near to the Fermi level (E_f) are reported and discussed in Section II.

Computational Details

High-throughput density functional theory (DFT)[54] calculations were performed with the Quantum Espresso simulation package[55] within the generalized gradient approximation proposed by Perdew, Burke, and Ernzerhof (PBE)[56]. We sampled the Brillouin zone (BZ) in the Monkhorst-Pack scheme[57], and tested the convergence in energy as a function of number of k-points for the calculations. The k-point sampling of $(7 \times 7 \times 1)$ was found to be suitable for the BZ corresponding to the primitive unit cell. Atomic positions were optimized using conjugate gradient method, where total energy and atomic forces were minimized. The energy convergence value between two consecutive steps was chosen as 10^4 eV. The energy interval chosen for density of states (DOS) calculations is 0.1 eV and the broadening used in Gaussian type. The standard value of broadening is considered as 0.001 Ry. An equivalent plane wave cutoff of 750 eV is chosen in all the simulations. Relaxed geometries are obtained with the conjugate gradient method, where all the atoms in the super cell are allowed to relax until the force on each atom is less than 0.02 eV/Å. We modeled the MoS_2/MoB_2 HS by putting a $3 \times 3 \times 1$ super cell of MoS_2 monolayer (lattice constant $a_{MoS_2} = 3.12$ Å)[58] on top of a $3 \times 3 \times 1$ super cell of MoB_2 monolayer ($a_{MoB_2} = 2.98$ Å)[53], which reduced the lattice mismatch between the two layers to 4.4% and resulted in a simulation cell containing 32 atoms. This lattice mismatch is small enough that will not effect the electronic properties of the HS, however such contraction in lattice spacings may results in increased DOS[16]. To minimize interactions between periodic images due to 3D boundary conditions, we introduced a vacuum layer such that the distance between periodic images was at least 25 Å. We have modeled the interaction of the valence electrons with the pseudo atomic cores of all the atomic species present in our studied structures by normconserving pseudopotentials explicitly including the semi-core Mo 4d electrons in the calculations. The equilibrium interfacial distance (d_{eq}) between MoS_2 and surface of MoB_2 monolayers is found to be 1.96 Å which is obtained from a fully relaxed HS. To analyze the thermoelectric properties of HS, semi-classical theory of the Boltzmann package[59] has been used.

Results and Discussion

Electronic Structure. *MoS_2/MoB_2 Heterostructure.* The lattice arrangement of the MoS_2/MoB_2 HS shown in Fig. 1 represents the clear existence of bonds at the interface between bottom S atoms and surface B atoms. These bonds indicates that the interaction among the atoms at the interface is not the Van der Waals interaction. In bulk, MoB_2 is a non-layered structure with metallic bonding[16,53] unlike MoS_2 which possess a layered structure with interlayer Van der Waals interaction. The metallic bonding of MoB_2 is possibly the reason for the absence of Van der Waals interaction at the interface of the HS. The electronic band structure of HS is shown in Fig. 2 where crossing of bands can be seen across the E_F showing the existence of metallic nature. The maximum dispersion of electronic bands is observed at high symmetry point M. In order to further elucidate the band structure we have studied the partial density of states (PDoS) of the HS. Figure 3 is showing the individual contributions of Mo atoms, (top/bottom) B atoms in MoB_2 (left panel) and similarly Mo and (top/bottom) S atoms in MoS_2 (right panel) along with total density of states (DoS) at the bottom. In Fig. 3, PDoS of MoB_2 (left) is shown, where 4d states of Mo atoms are found to cross the E_f. The PDoS of B atoms (below Mo) represents the 2p states which are also playing important role in the metallic nature of the HS. Whereas, PDoS of MoS_2 monolayer is represented in Fig. 3 (right). Here we find that, unlike the semiconducting nature of MoS_2 monolayer, 4d states of Mo are observed to cross over the E_f. However, the relative intensity of 4d states of Mo in MoS_2 monolayer (0.35 states/eV) is lower than that of 4d states of Mo in MoB_2 monolayer (0.47 states/eV) at E_f. 3p states of S atoms (below Mo) are also contributing in the metallic state of HS. The relative intensity of 3p states of S atoms in MoS_2 monolayer (0.11 states/eV) is lower than the 2p states of B atoms in MoB_2 monolayer (0.18 states/eV). From the above results obtained from Fig. 3, we conclude that the major contribution in the metallic character of MoS_2/MoB_2 HS is

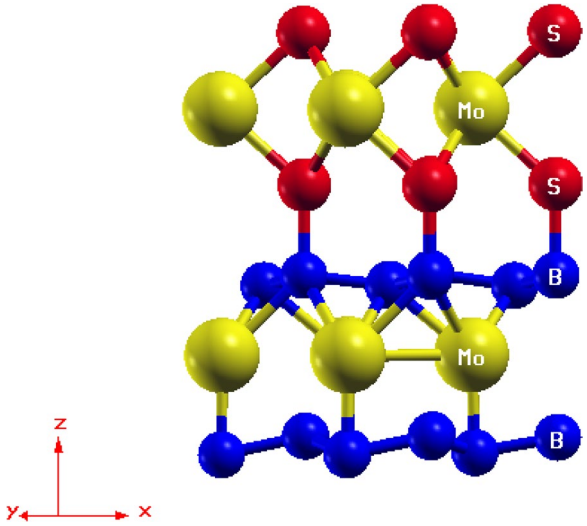

Figure 1. Lattice arrangement of MoS_2/MoB_2 HS. The formation of bonds at the interface is clearly visible.

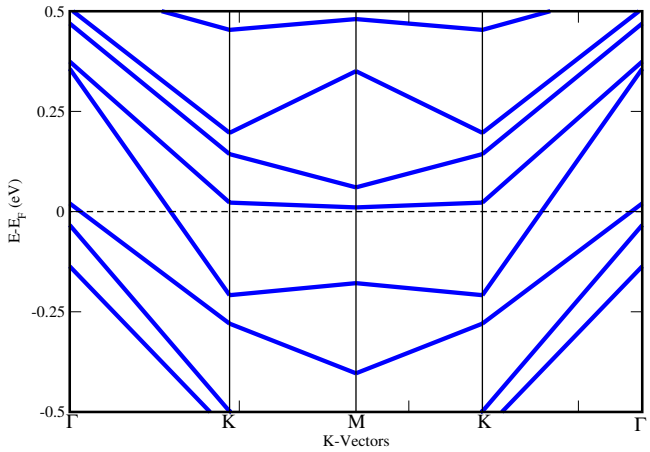

Figure 2. Electronic band structure of MoS_2/MoB_2 HS showing the metallic nature of the HS. The E_F is set to zero reference level.

attributed to Mo-4d and B-2p states of MoB_2 monolayer. MoB_2 is not only making the HS a metallic system but it has also modulated the MoS_2 monolayer to behave as a metallic system. The valance band (VB) in the range from −0.8 to −2 eV, is mainly composed of B-2p and Mo-4d (of MoB_2) states. Whereas, in the conduction band (CB), the energy range from 0.7 to 2 eV is mainly composed of Mo-4d states (of MoS_2 and MoB_2) and S-3p states. From energy range −0.7 to 0.5 eV, dominance of Mo-4d and B-2p states can be clearly seen in Fig. 3. The metallic nature in such type of HSs can be optimized for device applications like gas sensors based on resistivity alterations of the system. Band gaps obtained for other HSs based on MoS_2 are enlisted in Table 1. The PDoS diagrams of the sub-systems of the HS i.e. MoS_2 and MoB_2 are also studied to get a clear insight of the mechanism taking place within the HS and at its interface.

Subsystems: MoS_2 and MoB_2 Monolayers. To get a clear insight of electron transport, sub-systems (MoS_2 and MoB_2 monolayers) of the HS are also studied separately. The PDoS of MoS_2 monolayer in same lattice arrangement of HS, in absence of MoB_2 monolayer is shown in Fig. 4. We can see here that, when MoB_2 monolayer is not present, MoS_2 is giving an energy gap of 1.8 eV as expected from it[60]. 4d states of Mo and 3p states of S atoms are dominantly found in the CB near E_f level. The relative intensity of peaks of 4d states of Mo atoms (3.8 states/eV) are higher than that of 3p states of S atoms (1.6 states/eV). The PDoS of lower S atoms and top S atoms are identical. In the VB, there is a vacant space upto −1.7 eV which shows that the electronic states of MoS_2 monolayer are present in the VB in lower energy region ≤−1.7 eV. On observing Fig. 4, it is clear that, MoB_2 has strongly influenced the electronic states of MoS_2 monolayer when coupled together in the HS MoS_2/MoB_2 making it a metal. The PDoS of MoB_2 monolayer when MoS_2 monolayer is removed from the HS, is shown in Fig. 5. We can see here that 4d states of Mo are crossing the E_f level making it a metallic material. Below Mo, PDoS of bottom and top B atoms are shown. We found in Fig. 5 that 2p states of bottom B atoms are having higher intensity peaks at E_f as

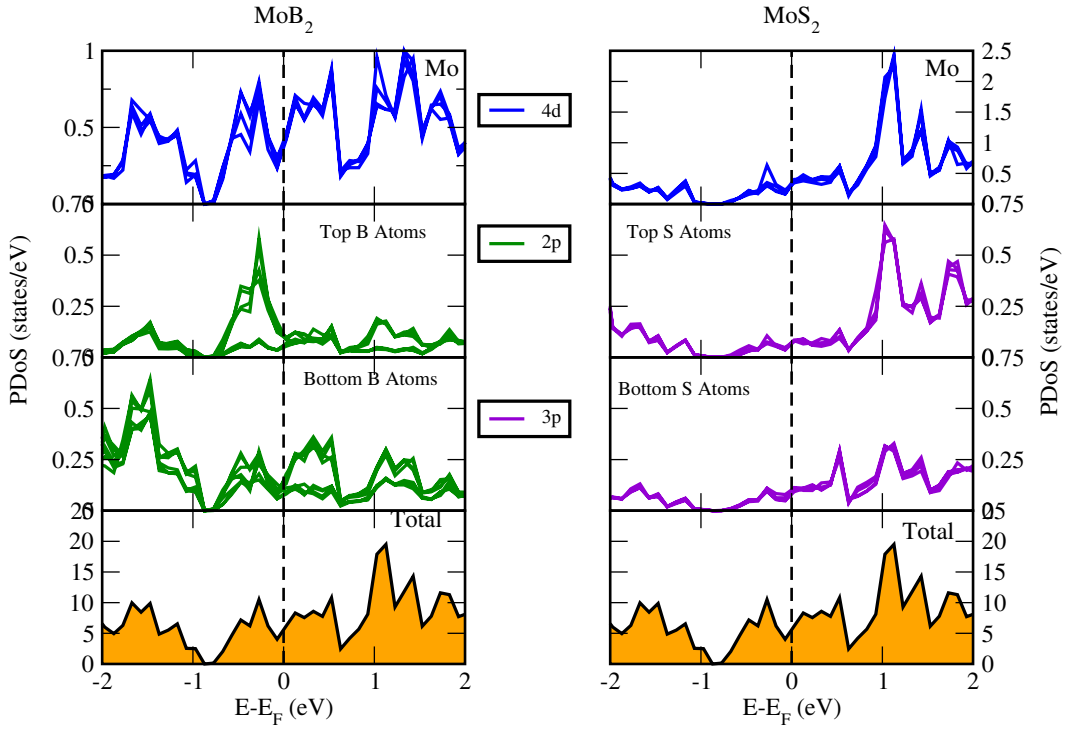

Figure 3. Projected density of states of MoS_2/MoB_2 HS. Left panel shows the contribution of MoB_2 and right panel shows the contribution of MoS_2 in the electronic structure of HS.

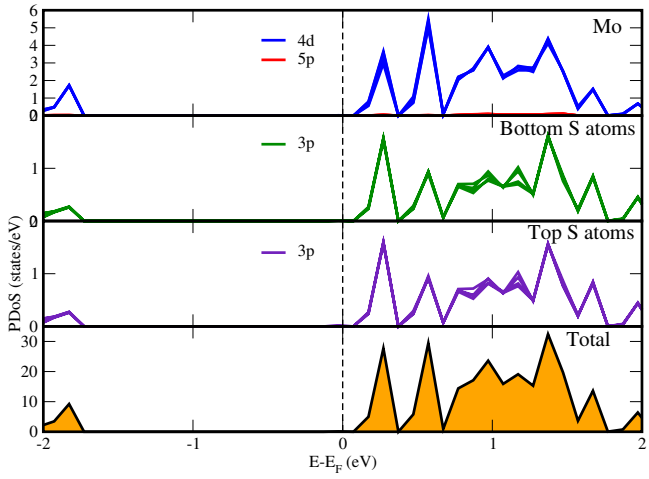

Figure 4. Projected density of states of MoS_2 monolayer on removing the MoB_2 layer from the HS.

compared to the top B atoms, which concludes that 2p states bottom B atoms are more actively participating with 4d states of Mo in making the system MoB_2 a metal. Our findings from Fig. 5 indicates that the interfacial bonds between MoS_2 and MoB_2 monolayers are metallic bonds.

Chemical Bonding. In the system of present investigation, we have performed the adsorption analysis of MoS_2 deposited on MoB_2 to confirm the metallic nature of interfacial bonding. In chemisorption the chemical reaction occurs between the surface of adsorbent (MoB_2) and adsorbate (MoS_2) and hence, new chemical bonds are generated at the interface along with consequential alterations in the electronic structure of adsorbate. On the other hand, in case of physisorption, the electronic properties of adsorbate remains unaltered upon adsorption. The bonds can be seen at the interface between adsorbent (MoB_2) and adsorbate (MoS_2) in Fig. 1. This MoB_2 driven modulation in the electronic structure of MoS_2 motivated us to investigate the nature of adsorption in MoS_2/MoB_2 HS system. In general, layered MoS_2 exhibits honeycomb like structure at the interface with Van der Waals like weak interactions. In our case we observed the existence of some ionic type bonding between B-2p electronic states of MoB_2 and S-3p electronic states of MoS_2 monolayers. Therefore it is considered that these

Heterostructure	Band Gap E_g (eV)
$MoSe_2/MoS_2$	0.74[15]
WS_2/MoS_2	1.16[15]
$FeSe_2/MoS_2$	Metal[15]
VS_2/MoS_2	Metal[15]
VSe_2/MoS_2	Metal[15]
$MoS_2/SrTiO_3$	0.85[27]
MoS_2/MoB_2	Metal *[This work]*

Table 1. Band gaps obtained in other works and present work.

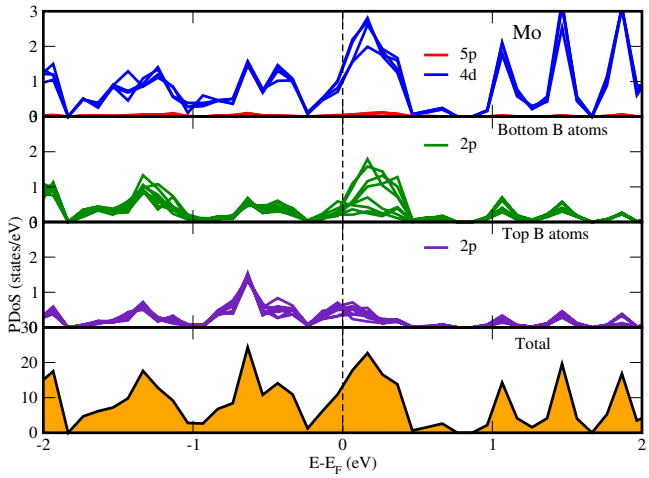

Figure 5. Projected density of states of MoB_2 monolayer on removing the MoS_2 layer from the HS.

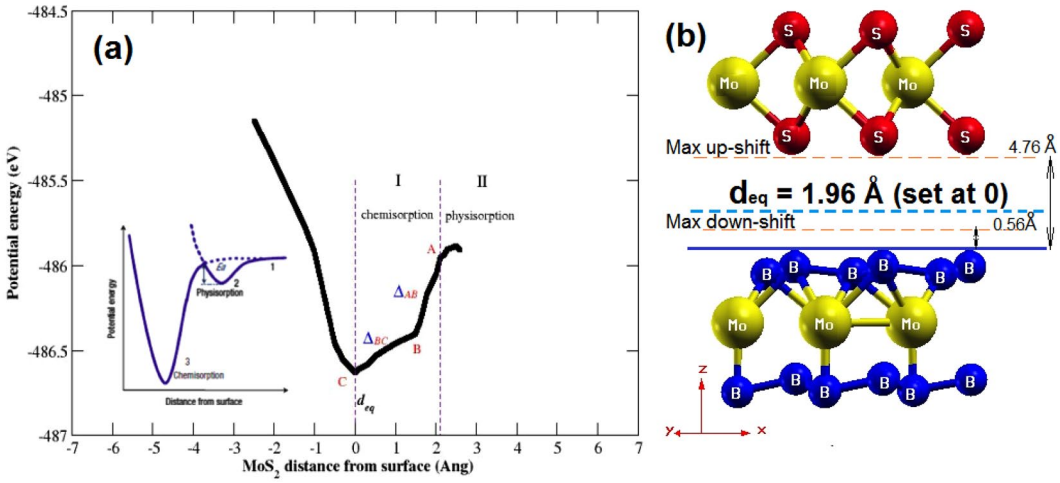

Figure 6. Nature of adsorption exists in the MoS_2/MoB_2 HS. Inset figure shows the ideal curve of adsorption.

interfacial interactions may not be the Van der Waals interactions[27]. In order to analyze the nature of adsorption at MoS_2/MoB_2 interface with equilibrium interfacial distance ($d_{eq} = 1.96\,Å$), we have randomly shifted MoS_2 monolayer upward upto 4.76 Å and then downward upto 0.56 Å normal to the plane of MoS_2/MoB_2 HS. The result obtained from adsorption curve in terms of change in potential energy with respect to interfacial distance is shown in Fig. 6(a), whereas the inset of Fig. 6(a) represents conventional potential energy versus interfacial distance curve. The diagrammatic representation of shifting of MoS_2 monolayer over MoB_2 is provided in Fig. 6(b). With reference to Fig. 6(b) the distance d_{eq} is set to 0 Å which indicates the minima of potential energy curve in Fig. 6(a). Again from Fig. 6(b) the maximum separation between MoS_2 and MoB_2 is ~4.76 Å which is then reduced to a minimum value ~0.56 Å. In Fig. 6(a) the two regions I and II can be allocated as chemisorption

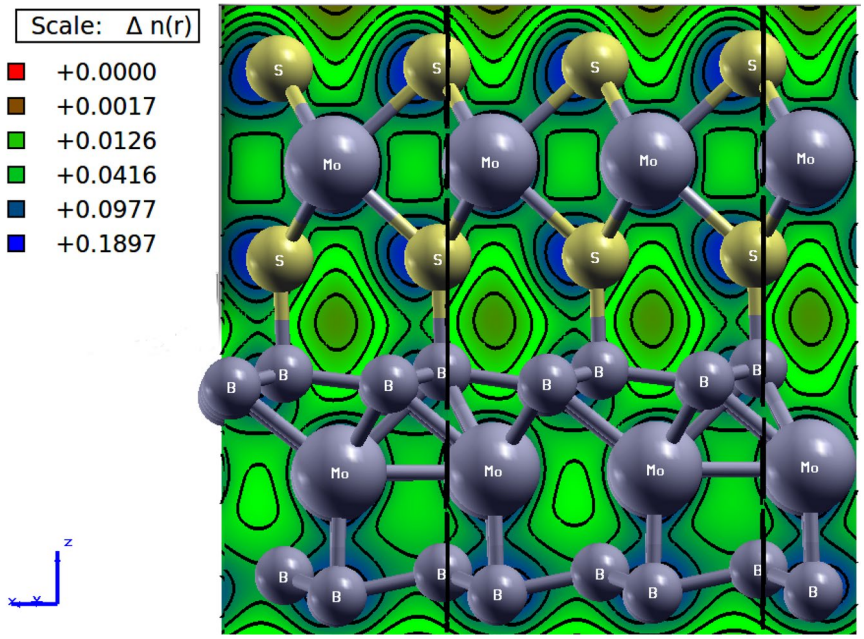

Figure 7. Charge density plot of MoS_2/MoB_2 HS in [010] plane.

and physisorption respectively. With reference to d_{eq}, the chemisorption occurs in the region from A (maxima at 2.1 Å) to C (minima at $d_{eq} = 1.96$ Å), where chemical bonds possibly exist at the interface of MoS_2/MoB_2 HS. The potential energy curve attains the minimum potential energy value (at C) by change in slope via point B. The rate of change of potential energy with respect to the interfacial distance between A and B i.e. Δ_{AB} is greater than that between B and C (Δ_{BC}). This variation in slope is attributed to initial electronic repulsion. In other words the anomaly at B in the potential energy curve appears due to electronic repulsion between MoS_2 and MoB_2 layers. Tending from B towards C the actual orbital overlapping between the atomic species of corresponding layers can be realized. Conclusively, at C in the potential energy curve the valley-like feature at d_{eq} indicates a clear existence of chemical bonding at the interface. If we further continue to decrease this distance, the energy will tend to infinity under the effect of nuclear repulsion. We can see from Fig. 6(a), that the trend of adsorption curve represents clear existence of chemical bonds at the interface which justify our results of electronic structure of HS and also confirms that the interfacial bonds are not merely the state-of-art. Now to show the nature of chemical bonding i.e. whether these bonds are metallic or covalent, we have further studied the charge density plot at the interface as shown in Fig. 7. Maximum value in the color plate on left shows the charge accumulation. Moreover the charge transfer occurs between top B atoms (of MoB_2 surface) and bottom S atoms (of MoS_2). This indicates the presence of strong bonding with metallic nature at the interface. Hybridization in Mo-4d states and B-2p states in the MoB_2 monolayer is also observed. In MoS_2 monolayer, Mo atoms weakly participate in charge transfer. These results are in good agreement with those observed for PDoS (Fig. 3) of MoS_2/MoB_2 HS. The isosurface plot of HS in Fig. 8 further elucidates the results of charge density. The interfacial bonding is clearly visible along with the bottom B atoms of the MoB_2 monolayer forming covalent B-B bonds among themselves[16] and surfacial B atoms (MoB_2 monolayer) making bonds with S atoms as well as B-B bonds.

Thermoelectric Properties. The performance of a thermoelectric material reflects in the dimensionless figure of merit $ZT = S^2\sigma T/\kappa$, where S is the Seebeck coefficient, σ is the electrical conductivity and κ ($\kappa = \kappa_e + \kappa_l$) is the thermal conductivity which consist electronic κ_e as well as lattice κ_l thermal conductivity and T is absolute temperature respectively. Previous studies signified that the mono-layered MoS_2 is semiconductor in nature with band gap 1.8 eV[60]. Due to high S and low κ, MoS_2 system presents a good candidature for the thermoelectric applications. However, small ZT is reported for this system due to low electrical conductivity induced by the large band gap energy. The mono-layered MoB_2 have metallic nature as represented in PDoS (Fig. 5) discussed in above section. We propose that wide band gap of MoS_2 semiconductor can be tuned by HS with MoB_2 that possibly results in enhanced power factor and thereby improve thermoelectric properties. Aiming this, we are the first to attempt the calculation and analysis of thermoelectric properties of MoS_2/MoB_2 HS using BoltzTrap code[59].

The Seebeck coefficient (S) as a function of chemical potential (μ) from −1.5 eV to 1.5 eV at temperatures 300 K and 800 K for MoS_2/MoB_2 HS show two peaks in the profile (Fig. 9a) which are located at a chemical potential near around −0.85 eV and −0.91 eV. It can be noticed that the resultant magnitude is larger for a p-type character. The maximum value of S is 134 μV/K, at 300 K which decreases with increasing temperature. The perpendicular component is higher in magnitude which is good for thermoelectric properties. The temperature dependence of Seebeck coefficient at a certain value of chemical potential is shown in Fig. 9(b). For MoS_2/MoB_2 HS the values of S in the entire temperature range are found to be positive which reveals that p-type charge carriers are dominant and increases with increasing temperature. Dimple *et al.*[41] observed the thermoelectric

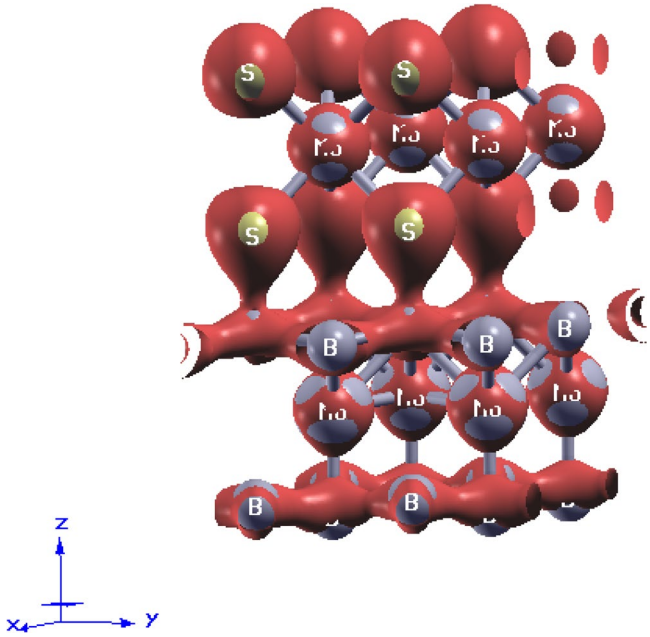

Figure 8. Isosurface results of MoS_2/MoB_2 HS showing the interfacial charge transfer between B-2p and S-3p orbitals.

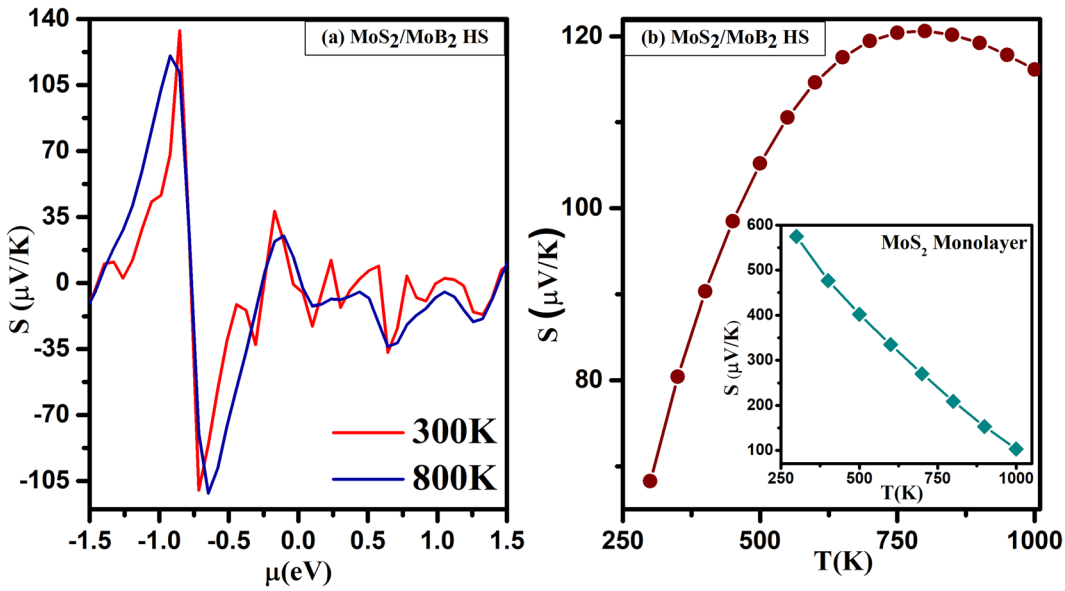

Figure 9. Seebeck coefficient (in μV/K, where $\mu = 10^{-6}$) varying as a function of (**a**) chemical potential μ (in eV) and (**b**) Temperature T(K) of MoS_2/MoB_2 HS and inset of (**b**) Temperature T(K) of MoS_2 Monolayer.

properties of MoS_2 monolayer which signify p-type character. However, the magnitude of S is very low ($=10^{-6}$) due to metallic nature of MoS_2/MoB_2 HS. The MoS_2 monolayer is a semiconductor that possess large band gap therefore its Seebeck coefficient must be larger than that of purely metallic MoB_2 which is shown in inset of Fig. 9(b). Moreover with reference to the electronic structure as discussed above for this HS, the band gap of MoS_2 monolayer is modulated by MoB_2. It can also be observed from PDoS of HS (Fig. 3) that the band gap of HS acquires metallic behavior and hence the Seebeck coefficient of mixed-layer MoS_2/MoB_2 is smaller than MoS_2 monolayer[61].

The variation of electrical conductivity (σ/τ) as a function of chemical potential (μ) from -2 eV to 2 eV at the temperatures 300 K and 800 K for MoS_2/MoB_2 HS is shown in Fig. 10(a). We have observed that the electrical conductivity for negative chemical potential is 3.73×10^{19} (S/ms) and 3.423×10^{19} (S/ms), whereas for positive chemical potential it is 5.21×10^{19} (S/ms) and 4.588×10^{19} (S/ms) for 300 K and 800 K respectively. This indicates that the p-type composition possess higher electrical conductivity than n-type. Comparable phenomena had also

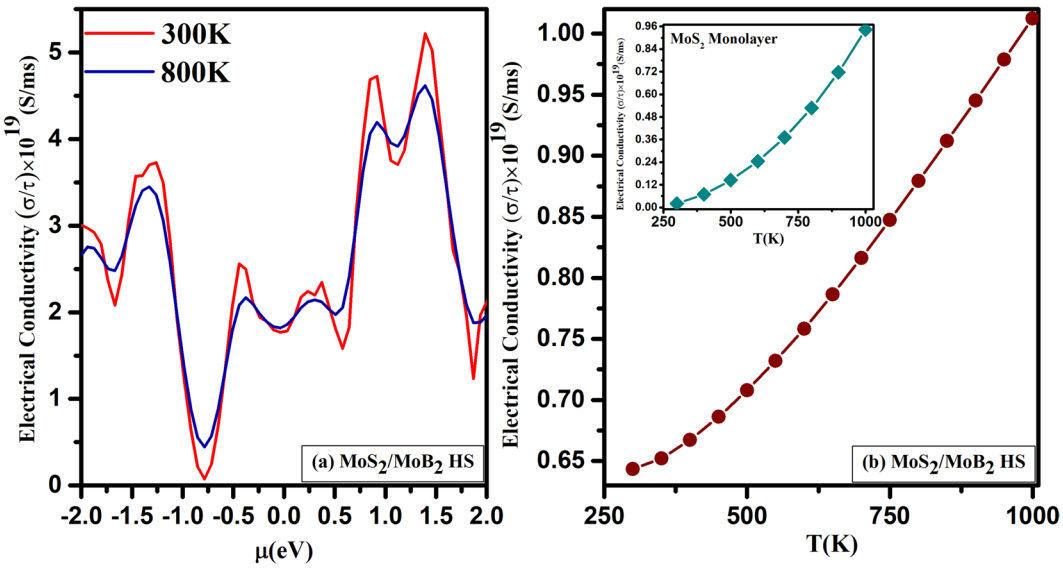

Figure 10. Electrical conductivity as a function of (**a**) chemical potential ($\mu(eV)$) and (**b**) Temperature T(K) of MoS_2/MoB_2 HS and inset of (**b**) Temperature T(K) of MoS_2 Monolayer.

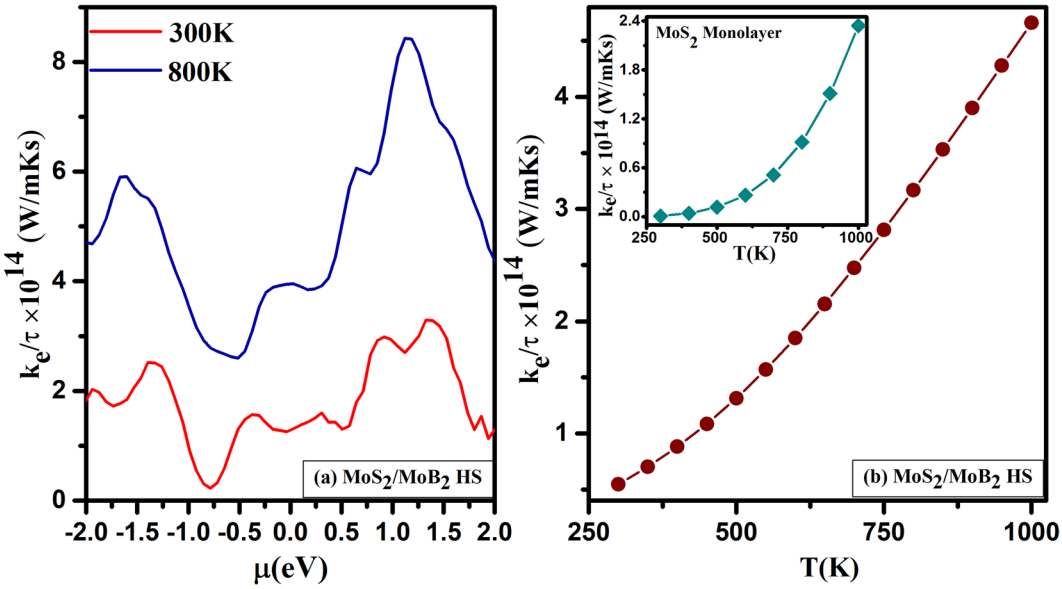

Figure 11. Thermal conductivity as a function of (**a**) chemical potential ($\mu(eV)$) and (**b**) Temperature T(K) of MoS_2/MoB_2 HS and inset of (**b**) Temperature T(K) of MoS_2 Monolayer.

been observed in MoS_2 monolayer[41]. Further, the electrical conductivity (σ/τ) as a function of temperature for a certain value of chemical potential (μ) is shown in Fig. 10(b). This figure shows that the electrical conductivity increases almost linearly with increasing temperature which indicates metallic nature, also confirmed by DoS study (Fig. 3). The electrical conductivity of MoS_2 monolayer have been provided in the inset of Fig. 10(b) which shows a similar trend like MoS_2/MoB_2 HS. However, the electrical conductivity of MoS_2 monolayer found lesser as compared to the investigated HS.

Further, we have also focused on the thermal conductivity of MoS_2/MoB_2 HS. In general, the thermal conductivity κ ($\kappa = \kappa_e + \kappa_l$) is a combination of electronic thermal conductivity κ_e and phononic thermal conductivity κ_l. In the present study, we have used the BoltzTrap code[59] which calculates electronic contribution only. The consideration of lattice thermal conductivity κ_l, remains as future task. The calculated electronic thermal conductivity (κ_e/τ) of MoS_2/MoB_2 HS as a function of chemical potential (μ) at 300 K and 800 K is shown in Fig. 11(a). It is indicated that a significant increase in κ_e/τ occurs with increasing temperature. The highest value of κ_e/τ induced by 800 K while the lowest κ_e/τ induced by 300 K. Therefore, 300 K is the optimal temperature that gives the lowest thermal conductivity. Moreover, the variation in thermal conductivity with respect to temperature is represented in Fig. 11(b). It shows a linear dependence with respect to temperature because the increasing

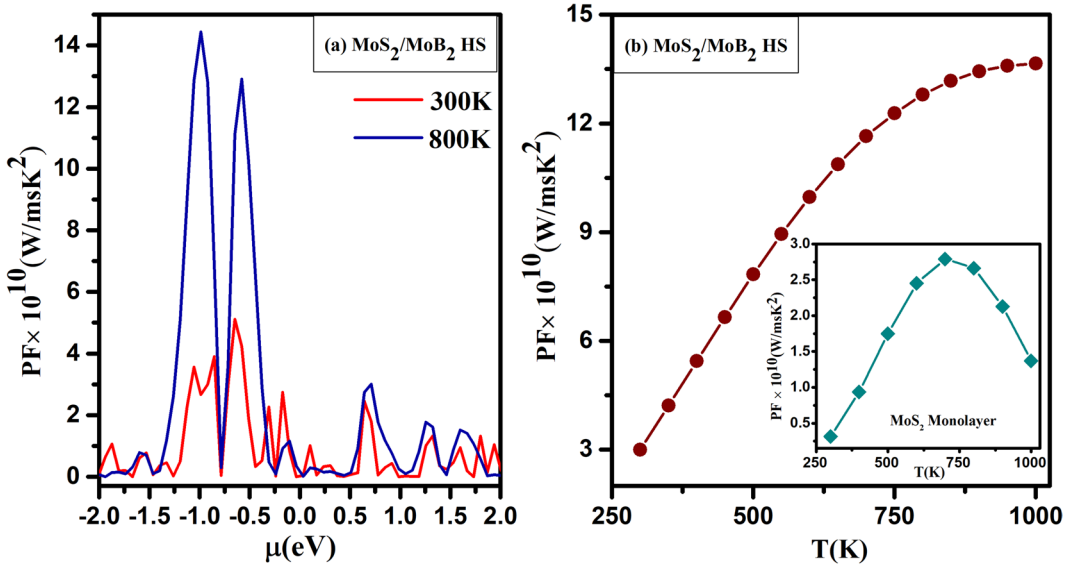

Figure 12. Power factor as a function of (**a**) chemical potential ($\mu(eV)$) and (**b**) Temperature T(K) of MoS_2/MoB_2 HS and inset of (**b**) Temperature T(K) of MoS_2 Monolayer.

temperature enhances the number of charge carriers attributed to the metallic nature of MoS_2/MoB_2 HS which is in good agreement with the previous study[62]. However, the thermal conductivity of MoS_2 is found less as compared to that of MoS_2/MoB_2 HS as shown in the inset of Fig. 11(b). It is due to the large band gap semiconducting nature of MoS_2 monolayer[63].

The average power factor is plotted against the chemical potential (μ) at 300 K and 800 K illustrated in Fig. 12(a). The positive (and negative) chemical potential scale indicates the electron (and hole) concentration, respectively. The power factor is maximum near $\mu = -0.99$ eV attributed to significant increment in the electrical conductivity at high electron concentration level. Further, Fig. 12(b) represents the power factor with respect to increasing temperature which initially increases rapidly and then becomes almost linear till 1000 K. The comparative power factor of MoS_2 monolayer is shown in the inset of Fig. 12(b). It is clear that the investigated MoS_2/MoB_2 HS exhibits comparatively better power factor value than MoS_2 monolayer. The large magnitude of power factor is obtained in the case of large electrical conductivity. Consequently, it is clear that the heterostructure of MoS_2/MoB_2 HS exhibit good thermoelectric response at the higher temperatures.

Conclusions

In conclusion, our study suggests that deposition of MoS_2 monolayer over single layer of MoB_2 in a bilayer MoS_2/MoB_2 heterostructure can have noticeable effects on the electronic properties of the MoS_2 layer. In presence of MoB_2 layer in the HS, monolayer of MoS_2 becomes a metallic system. Under the influence of 4d and 2p states of Mo and B atoms respectively of MoB_2 layer, 4d and 3p states of Mo and S atoms of MoS_2 monolayer appeared to cross the E_f. While in absence of MoB_2 layer, MoS_2 monolayer shows its ideal electronic structure. Hence the metallic nature of the HS is driven by MoB_2 layer. We also observed some bonds at the interface which were analyzed via charge density calculation and adsorption curve and found to be metallic in nature. Based on the calculated Seebeck effect and power factor of MoS_2/MoB_2 HS as a function of chemical potential and temperature, the maximum power factor is estimated successfully which can offer useful guidelines for tuning and improving the thermoelectric performance of such type of HS.

References

1. Radisavljevic, B., Radenovic, A., Brivio, J., Giacometti, V. & Kis, A. Single-layer MoS_2 transistors. *Nature Nanotechnol.* **6**, 147–150 (2011).
2. Kim, S. *et al.* High-mobility and low-power thin-film transistors based on multilayer MoS_2 crystals. *Nature Commun.* **3**, 1011, https://doi.org/10.1038/ncomms2018 (2012).
3. Lembke, D. & Kis, A. Breakdown of High-Performance Monolayer MoS_2 Transistors. *ACS Nano* **6**, 10070–10075 (2012).
4. Sangwan, V. K. *et al.* Low-frequency electronic noise in single-layer MoS_2 transistors. *Nano Lett.* **13**, 4351–4355 (2013).
5. Wang, Q. H., Kalantar-Zadeh, K., Kis, A., Coleman, J. N. & Strano, M. S. Electronics and optoelectronics of two-dimensional transition metal dichalcogenides. *Nature Nanotechnol.* **7**, 699–712 (2012).
6. Lee, H. S. MoS_2 nanosheet phototransistors with thickness-modulated optical energy gap. *Nano Lett.* **12**, 3695–3700 (2012).
7. Zhang, W. *et al.* Ultrahigh-gain photodetectors based on atomically thin graphene-MoS_2 heterostructures. *Sci. Rep.* **4**, 3826, https://doi.org/10.1038/srep03826 (2014).
8. Roy, K. *et al.* Graphene-MoS_2 hybrid structures for multifunctional photoresponsive memory devices. *Nature Nanotechnol.* **8**, 826–830 (2013).
9. Terrones, H., López-Urias, F. & Terrones, M. Novel hetero-layered materials with tunable direct band gaps by sandwiching different metal disulfides and diselenides. *Sci. Rep.* **3**, 1549, https://doi.org/10.1038/srep01549 (2013).
10. Novoselov, K. S. & Castro Neto, A. H. Two-dimensional crystals-based heterostructures: materials with tailored properties. *Phys. Scr.* **T146**, 014006, https://doi.org/10.1088/0031-8949/2012/T146/014006 (2012).

11. Gillen, R., Robertson, J. & Maultzsch, J. Indirect doping effects from impurities in MoS_2/h-BN heterostructures. *Phys. Rev. B* **90**, 075437, https://doi.org/10.1103/PhysRevB.90.075437 (2014).
12. Wang, H. *et al*. Integrated circuits based on bilayer MoS_2 transistors. *Nano Lett.* **12**, 4674–4680 (2012).
13. Radisavljevic, B., Whitwick, M. & Kis, A. Integrated circuits and logic operations based on single-layer MoS_2. *ACS Nano* **5**, 9934–9938 (2011).
14. Geim, A. & Grigorieva, I. Van der Waals heterostructures. *Nature* **499**, 419–425 (2013).
15. Lu, N. *et al*. MoS_2/MX_2 heterobilayers: bandgap engineering via tensile strain or external electrical field. *Nanoscale* **6**, 2879–2886 (2014).
16. Paduani, C. Electronic structure of magnesium diboride and related compounds. *Phys. Stat. Sol. (B)* **240**, 574–583 (2003).
17. Hu, T. & Hong, J. Anisotropic effective mass, optical property, and enhanced band gap in BN/Phosphorene/BN heterostructures. *J. ACS Appl. Mater. Interfaces* **7**, 23489–23495 (2015).
18. Lu, J. *et al*. Phosphorene: enhanced photoresponse from phosphorene-phosphorene-suboxide junction fashioned by focused laser micromachining. *Adv. Mater.* **28**, 4164, https://doi.org/10.1002/adma.201670146. (2016).
19. Zhao, Y. *et al*. Surface coordination of black phosphorus for robust air and water stability. *Angew. Chem. Int. Ed.* **55**, 5003–5007 (2016).
20. Guo, G. C. *et al*. First-principles study of phosphorene and graphene heterostructure as anode materials for rechargeable Li batteries. *J. Phys. Chem. Lett.* **6**, 5002–5008 (2015).
21. Dai, J. & Zeng, X. C. Bilayer phosphorene: effect of stacking order on bandgap and its potential applications in thin-film solar cells. *J. Phys. Chem. Lett.* **5**, 1289–1293 (2014).
22. Huang, L. & Li, J. Tunable electronic structure of black phosphorus/blue phosphorus van der Waals p-n heterostructure. *Appl. Phys. Lett.* **108**, 083101, https://doi.org/10.1063/1.4942368 (2016).
23. Hu, X. R., Zhengy, J. M. & Ren, Z. Y. Strong interlayer coupling in phosphorene/graphene van der Waals heterostructure: A first-principles investigation. *Front. Phys.* **13**, 137302, https://doi.org/10.1007/s11467-017-0736-0 (2018).
24. Shim, G. W. *et al*. Large-area single-layer $MoSe_2$ and its van der Waals heterostructures. *ACS Nano* **8**, 6655–6662 (2014).
25. You, B., Wang, X., Zheng, Z. & Mi, W. Black phosphorene/monolayer transition-metal dichalcogenides as two dimensional van der Waals heterostructures: a first-principles study. *Phys. Chem. Chem. Phys.* **18**, 7381–7388 (2016).
26. Kaur, S., Kumar, A., Srivastava, S. & Tankeshwar, K. Van der Waals heterostructures based on allotropes of phosphorene and $MoSe_2$. *Phys. Chem. Chem. Phys.* **19**, 22023–22032 (2017).
27. Bano, A. & Gaur, N. K. Interfacial Coupling Effect on Electron Transport in $MoS_2/SrTiO_3$ Heterostructure: An Ab-initio Study. *Sci. Rep.* **8**, 714, https://doi.org/10.1038/s41598-017-18984-6 (2018).
28. Boggs, D. S. & Krinsley, D. Application of cathodoluminescence imaging to the study of sedimentary rocks (Cambridge University Press, 2006).
29. Chin, A. K., Zipfel, C. L., Mahajan, S., Ermanis, F. & Digiuseppe, M. A. Cathodoluminescence evaluation of dark spot defects in InP/InGaAsP light-emitting diodes. *Appl. Phys. Lett.* **41**, 555, https://doi.org/10.1063/1.93602 (1982).
30. Griffiths, J. T. *et al*. Nano-cathodoluminescence reveals the effect of electron damage on the optical properties of nitride optoelectronics and the damage threshold. *Nano Lett.* **15**, 7639, https://doi.org/10.1063/1.4965989 (2015).
31. Zhao, M. *et al*. Visible surface plasmon modes in single Bi_2Te_3 nanoplate. *Nano Lett.* **15**, 8331–8335 (2015).
32. Ruf, T. *et al*. Cathodoluminescence investigation of isotope effects in diamond. *Solid State Commun.* **105**, 311–316 (1998).
33. Watanabe, K., Taniguchi, T. & Kanda, H. Direct-bandgap properties and evidence for ultraviolet lasing of hexagonal boron nitride single crystal. *Nat. Mater.* **3**, 404–409 (2004).
34. Bhattacharyya, S., Tribhuwan, P. & Singh, A. K. Effect of strain on electronic and thermoelectric properties of few layers to bulk MoS_2. *Nanotechnology* **25**, 465701, https://doi.org/10.1088/0957-4484/25/46/465701 (2014).
35. Wickramaratne, D., Zahid, F. & Lake, R. K. Electronic and thermoelectric properties of few-layer transition metal dichalcogenides. *J. Chem. Phys.* **140**, 124710, https://doi.org/10.1063/1.4869142 (2014).
36. Huang, W., Luo, X., Gan, C. K., Quek, S. Y. & Liang, G. Theoretical study of thermoelectric properties of few-layer MoS_2 and WSe_2. *Phys. Chem. Chem. Phys.* **16**, 10866–108874 (2014).
37. Jin, Z. *et al*. A revisit to high thermoelectric performance of single-layer MoS_2. *Sci. Rep.* **5**, 18342, https://doi.org/10.1038/srep18342 (2015).
38. Hippalgaonkar, K. *et al*. High thermoelectric powerfactor in single and few-layer MoS_2. *Phys. Rev. B* **95**, 115407, https://doi.org/10.1103/PhysRevB.95.115407 (2017).
39. Babaei, H., Khodadadi, J. M. & Sinha, S. Large theoretical thermoelectric power factor of suspended single-layer MoS_2. *Appl. Phys. Lett.* **105**, 193901, https://doi.org/10.1063/1.4901342 (2014).
40. Zhang, Z., Xie, Y., Peng, Q. & Chen, Y. A theoretical prediction of super high-performance thermoelectric materials based on MoS_2/WS_2 hybrid nanoribbons. *Sci. Rep.* **6**, 21639, https://doi.org/10.1038/srep21639 (2016).
41. Dimple, Jena, N. & Sarkar, A. D. Compressive strain induced enhancement in thermoelectric-power-factor in monolayer MoS_2 nanosheet. *J. Phys.: Condens. Matter* **29**, 225501, https://doi.org/10.1088/1361-648X/aa6cbc (2017).
42. Varin, R. A., Chiu, C., Li, S., Calka, A. & Wexler, D. Application of controlled and electrical discharge assisted mechanical alloying for the synthesis of nanocrystalline MgB_2 superconducting compound. *J. Alloys Compd.* **370**, 230–243 (2004).
43. Erdemir, A., Halter, M. & Fenske, G. R. Preparation of ultralow-friction surface films on vanadium diboride. *Wear* **205**, 236–239 (1997).
44. Shein, I. R. & Ivanovskii, A. L. Influence of lattice vacancies on the structural, electronic, and cohesive properties of niobium and molybdenum borides from first-principles calculations. *Phys. Rev. B* **73**, 144108, https://doi.org/10.1103/PhysRevB.73.144108 (2006).
45. Deligoz, E., Colakoglu, K. & Ciftci, Y. O. Lattice dynamical properties of ScB_2, TiB_2, and VB_2 compounds. *Solid State Commun.* **149**, 1843–1848 (2009).
46. Zhou, W., Wu, H. & Yildirim, T. Electronic, dynamical, and thermal properties of ultra-incompressible superhard rhenium diboride: A combined first-principles and neutron scattering study. *Phys. Rev. B* **76**, 184113, https://doi.org/10.1103/PhysRevB.76.184113 (2007).
47. Chung, H. Y., Weinberger, M. B. & Levine, J. B. Synthesis of ultra-incompressible superhard rhenium diboride at ambient pressure. *Science* **316**, 436–439 (2007).
48. Cumberland, R. W., Weinberger, M. B. & Gilman, J. J. Osmium diboride, an ultra-incompressible, hard material. *J. Am. Chem. Soc.* **127**, 7264, https://doi.org/10.1021/ja043806y (2005).
49. Suda, J. & Matsunami, H. Heteroepitaxial growth of group-III nitrides on lattice-matched metal boride ZrB_2 (0 0 0 1) by molecular beam epitaxy. *J. Cryst. Growth* **237**, 1114–1117 (2002).
50. Yamada-Takamura, Y. *et al*. *Phys. Rev. Lett.* **95**, 266105, https://doi.org/10.1103/PhysRevLett.95.266105 (2005).
51. Kulikowski, Z. *et al*. Mechanical and microstructural behaviour of a particulate reinforced steel for structural applications. *Mater. Sci. Technol.* **16**, 1453–1464 (2000).
52. Qi, C. J., Jiangn, Y. H., Liu, Y. Z. & Zhou, R. Elastic and electronic properties of XB_2 (X = V, Nb, Ta, Cr, Mo, and W) with AlB_2 structure from first principles calculations. *Ceram. Int.* **40**, 5843–5851 (2014).
53. Qin, N., Liu, S-Y., Zhao, H. & Wang, S. First-principles studies for the stability of a graphene-like boron layer on CrB_2 (0001) and MoB_2 (0001). *J. Phys.: Condens. Matter* **23**, https://doi.org/10.1088/0953-8984/23/22/225501 (2011).

54. Hohenberg, P. & Kohn, W. Inhomogeneous Electron Gas. *Phys. Rev.* **136**, B864, https://doi.org/10.1103/PhysRev.136.B864 (1964).
55. Giannozzi, P. *et al*. QUANTUM ESPRESSO: a modular and open-source software project for quantum simulations of materials. *J.Phys.:Condens. Matter* **21**, 395502, https://doi.org/10.1088/0953-8984/21/39/395502 (2009).
56. Perdew, J. P., Burke, K. & Ernzerhof, M. Generalized gradient approximation made simple. *Phys. Rev. Lett.* **77**, 3865, https://doi.org/10.1103/PhysRevLett.77.3865 (1996).
57. Monkhorst, H. J. & Pack, J. D. Special points for Brillouin-zone integrations. *Phys. Rev. B* **13**, 5188, https://doi.org/10.1103/PhysRevB.13.5188 (1976).
58. Wakabayashi, N., Smith, H. G. & Nicklow, R. M. Lattice dynamics of hexagonal MoS_2 studied by neutron scattering. *Phys. Rev. B* **12**, https://doi.org/10.1103/PhysRevB.12.659 (1975).
59. Madsen, G. K. H. & Singh, D. J. BoltzTraP. A code for calculating band-structure dependent quantities. *Comput. Phys. Commun.* **175**, 67–71 (2006).
60. Mak, K. F., Lee, C., Hone, J., Shan, J. & Heinz, T. F. Atomically thin MoS_2: A new direct-gap semiconductor. *Phys. Rev. Lett.* **105**, 136805, *arxiv.org/pdf/1004.0546.pdf* (2010).
61. Lee, C., Hong, J., Lee, W. R., Kim, D. Y. & Shim, J. H. Density functional theory investigation of the electronic structure and thermoelectric properties of layered MoS_2, $MoSe_2$ and their mixed-layer compound. *J. Solid State Chem.* **211**, 113–119 (2014).
62. Rai, D. P. *et al*. Electronic, optical and thermoelectric properties of $Fe_{2+x}V_{1-x}Al$. *AIP Adv.* **7**, 045118, https://doi.org/10.1063/1.4982671 (2017).
63. Padilha, J. E., Fazzio, A. & da Silva, A. J. Van der Waals heterostructure of phosphorene and graphene: tuning the Schottky barrier and doping by electrostatic gating. *Phys. Rev. Lett.* **114**, 066803, https://doi.org/10.1103/PhysRevLett.114.066803 (2015).

Acknowledgements
The authors are thankful to University Grants Commission (UGC), New Delhi for providing the financial support.

Author Contributions
A.B. performed structure modeling and calculations. Authors A.B. and D.K.P. analyzed interfacial electronic structure and adsorption curve. A.M. performed thermoelectric properties analysis. N.K.G. provided major corrections to the manuscript. All the authors discussed the results and reviewed the manuscript.

Additional Information
Competing Interests: The authors declare no competing interests.

Publisher's note: Springer Nature remains neutral with regard to jurisdictional claims in published maps and institutional affiliations.

Open Access This article is licensed under a Creative Commons Attribution 4.0 International License, which permits use, sharing, adaptation, distribution and reproduction in any medium or format, as long as you give appropriate credit to the original author(s) and the source, provide a link to the Creative Commons license, and indicate if changes were made. The images or other third party material in this article are included in the article's Creative Commons license, unless indicated otherwise in a credit line to the material. If material is not included in the article's Creative Commons license and your intended use is not permitted by statutory regulation or exceeds the permitted use, you will need to obtain permission directly from the copyright holder. To view a copy of this license, visit http://creativecommons.org/licenses/by/4.0/.

© The Author(s) 2018